Investigation of Criterion for Applying Incident Power Density in The Near-field Region for EMF Assessment at Quasi-Millimeter and Millimeter-Wave Frequencies

Yao, Ming; Pedersen, Gert Frølund; Zhang, Shuai

Published in:
I E E E Transactions on Electromagnetic Compatibility

DOI (link to publication from Publisher):
10.1109/TEMC.2024.3371066

Publication date:
2024

Document Version
Accepted author manuscript, peer reviewed version

Investigation of Criterion for Applying Incident Power Density in The Near-field Region for EMF Assessment at Quasi-Millimeter and Millimeter-Wave Frequencies

Ming Yao, *Graduate Student Member, IEEE,* Gert Frølund Pedersen, *Senior Member, IEEE*, and Shuai Zhang, *Senior Member, IEEE*

***Abstract*—In the international electromagnetic field (EMF) exposure guidelines revised in the year 2020, the absorbed power density (APD) and the incident power density (IPD) are the exposure quantities that can be used to determine compliance above 6 GHz for local exposure. It is indicated in the guidelines that the IPD, a quantity to be assessed in free space, cannot be used for compliance assessment in the reactive near field of the antenna of the equipment under the test. In such a condition, the APD, the quantity to be assessed inside the human body, should be used. The reason stated in the guidelines is that the IPD does not appropriately correlate with APD in the reactive near field. However, the guidelines do not explicitly specify the criteria or computation method that can be applied to determine such boundary. Although the rough guide of $\lambda/2\pi$ is mentioned, it may be too small and not suitable for EMF assessment of practical user equipment under test. This paper investigates a criterion and method for determining the boundary for applying the IPD in the near field. It has been demonstrated by the analytical solution for an infinitesimal dipole antenna, simulated and measured results for practical antenna arrays. For the studied antennas, the results show that the boundary determined by the proposed method could better represent the transition from the reactive near field to the radiation near field compared to the classical reactive near-field boundary when examining the correlation between IPD and APD for EMF assessment.**

***Index Terms*—EMF assessment, incident power density, absorbed power density, near field region.**

I. Introduction

THE electromagnetic field (EMF) exposure from user equipment has attracted public attention as communication technologies develop rapidly [1]. The EMF exposure limits have been published to protect human health, e.g., in the most widely used ICNIRP guidelines covering the frequency range from 100 kHz to 300 GHz [2]. One set of EMF exposure limits provided in the ICNIRP guidelines is named basic restrictions, which are derived from the associated heating effects of the human body with great safety margins. They are determined for whole-body and local exposure to restrict the core and local temperature rise in the human body.

This work done by Ming Yao was supported in part by the China Scholarship Council. (*Corresponding author: Shuai Zhang*)

Ming Yao, Gert Frølund Pedersen, and Shuai Zhang are with the Antenna, Propagation and Millimeter-Wave Systems Section, Department of Electronic Systems, Aalborg University, 9220 Aalborg, Denmark (e-mail: sz@es.aau.dk).

The basic restrictions for local exposure averaged for 6 min are defined in terms of specific absorption rate (SAR) averaged over a mass of 10 g of human tissue below 6 GHz. Above 6 GHz, the absorbed power density (APD) should be used. The basic restrictions are defined as quantities inside the human body [2]. To restrict the temperature rise, some studies on APD, e.g., [3], [4], and the relationship between APD and the temperature rise in the different human body models have been reported, e.g., [5]–[11]. In [2], it is indicated that APD should be averaged over $4\ \mathrm{cm}^2$ for frequencies ranging from 6 to 300 GHz and $1\ \mathrm{cm}^2$ for frequencies ranging from 30 to 300 GHz to better correlate with temperature rise in the human body. The other set of EMF exposure limits, namely reference levels, is derived from the basic restrictions based on worst-case scenarios. Above 6 GHz, they are defined in terms of incident power density (IPD), which is a quantity to be assessed in free space [2].

Originally, IPD represents the directional energy flux, which is the energy transferred per unit area per unit time, expressed as the real part of the complex Poynting vector. Nevertheless, some studies, e.g., [12], [13], suggest that the norm of the IPD might be considered instead for EMF compliance assessment. There have been many studies provide comparisons of correlation of different IPD expressions with tissue temperature rise when the evaluation distances are close to the antennas, e.g., [14]–[21]. These studies indicate that the difference between two IPD expressions is relatively marginal when the evaluation distance is larger than a certain value. More recently, another expression of IPD using the norm of the complex Poynting vector considering both the real and imaginary parts was proposed in [22]. It should be noticed that these expressions provide the same value in the far field if the averaging area for IPD assessment is perpendicular to the wave propagation direction.

As mentioned above, IPD has attracted more interest and is more commonly used for EMF compliance assessment as it is assessed in free space and is easier to evaluate compared to the APD assessed within the tissue. However, [2] stated that IPD cannot be used to determine compliance in the reactive near field because the IPD limits are derived from the APD limits under the plane-wave condition, i.e., in the far field. In the reactive near field, it is stated in the guidelines that the IPD does not appropriately correlate with APD. It is also mentioned

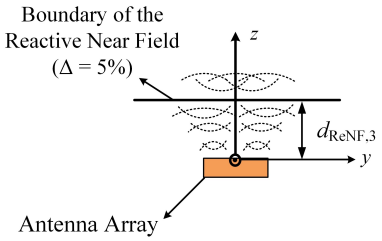

Fig. 1. Side view illustration of the proposed reactive near field.

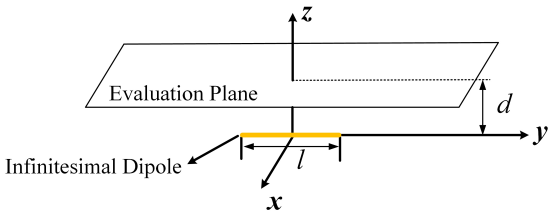

Fig. 2. Illustration of the evaluation plane at a distance d from the infinitesimal dipole with a length of l =0.01λ operating at frequency of 28 GHz. The dimension of the evaluation plane is 100 mm × 100 mm.

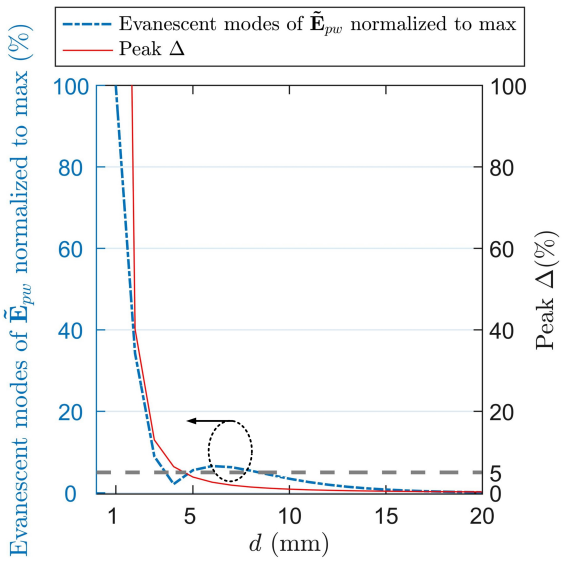

Fig. 3. Evanescent modes of $\tilde{\mathbf{E}}_{pw}$ (percentage) normalized to the maximum value and peak Δ (percentage) at separation distances from 1–20 mm. The maximum value (represented as 100% in this figure) for the normalized evanescent modes of $\tilde{\mathbf{E}}_{pw}$ corresponds to d = 1 mm, and the gray dashed line corresponds to 5%.

that there is no explicit delineation of how far the reactive near field should extend to ensure that IPD can be applied for EMF assessments. Although a rough guide is provided, it might be too small and not suitable for EMF assessment in practical user equipment under test. The definition of the rough guide and the other classical widely-used criteria are [2], [23], [24]

$$d_{\mathrm{ReNF}_1} = \frac{\lambda}{2\pi}, \tag{1}$$

$$d_{\mathrm{ReNF}_2} = 0.62\sqrt{\frac{D^3}{\lambda}}, \tag{2}$$

where λ is the wavelength in free space, and D is the largest dimension of the antenna.

The distance in (1) is where the real part of the power flux is equal to the imaginary part using an ideal infinitesimal dipole [23]. The distance in (2) is derived by arbitrarily letting the maximum phase error equal to or less than $\pi/8$ using a finite dipole of any length [23, Eq. (4-51)]. Nevertheless, the above definitions of the reactive near-field boundary are derived from ideal dipole antennas. The criteria should be different when evaluating whether IPD is suitable to be applied at a certain close distance of a more practical antenna or antenna array for EMF assessments. Some recent studies, e.g., [25], focusing on computational methods for analyzing the field regions, have also shown that the classical criterion may not be applicable for large practical antenna structures. Moreover, determining such field region boundary should also be related to beam-scanning of antenna arrays, which are typically used in 5G mmWave devices [14]. Therefore, the motivation of this work is to investigate a criterion and method for determining the extent of the reactive near-field boundary for EMF assessment. Outside this boundary, IPD as the reference levels can be applied. Conversely, APD should be used inside the boundary.

The organization of this paper is as follows: Section II states the proposition of the method and criterion for determining the reactive near-field boundary by using the evaluated electromagnetic fields. It also includes the demonstration of the effectiveness of the method. Additionally, some simulation and measurement settings are introduced. In Section III, simulations and measurements for practical antennas are performed to further demonstrate the proposed method. In section IV, the relationship between IPD and APD is examined inside and outside the boundary determined by the proposed method, which aims to study whether IPD can be applied to EMF assessment. In Section V, some discussions and conclusions are presented.

II. Methodology and Models

A. Definitions of IPD

It is well known that integration of the complex Poynting vector over a closed surface s immediately adjacent to and surrounding the antenna yields [26]

$$\frac{1}{2}\oint_s (\boldsymbol{E}\times\boldsymbol{H}^*)\cdot \mathrm{d}\boldsymbol{s} = P + 2j\omega\left(W_{\mathrm{m}} - W_{\mathrm{e}}\right), \tag{3}$$

where $\boldsymbol{E}$ and $\boldsymbol{H}$ are the complex electric and magnetic fields, respectively, $*$ is conjugation, $\boldsymbol{s}$ is the vector area, P is the radiated power, ω is the angular frequency, and W_{e} and W_{m} are the stored electric and magnetic energy densities, respectively. The real part of the complex Poynting vector integrated over the closed surface gives the radiated power P, while the imaginary part is the net stored energy in the field. The imaginary part decays to zero in the far field.

When evaluating IPD averaged over an area, it is natural to use the component normal to the area as its integration represents the net energy flux

$$S_{\mathrm{inc},1} = \frac{1}{2}\mathrm{Re}(\boldsymbol{E}\times\boldsymbol{H}^*)\cdot\hat{\boldsymbol{n}}, \tag{4}$$

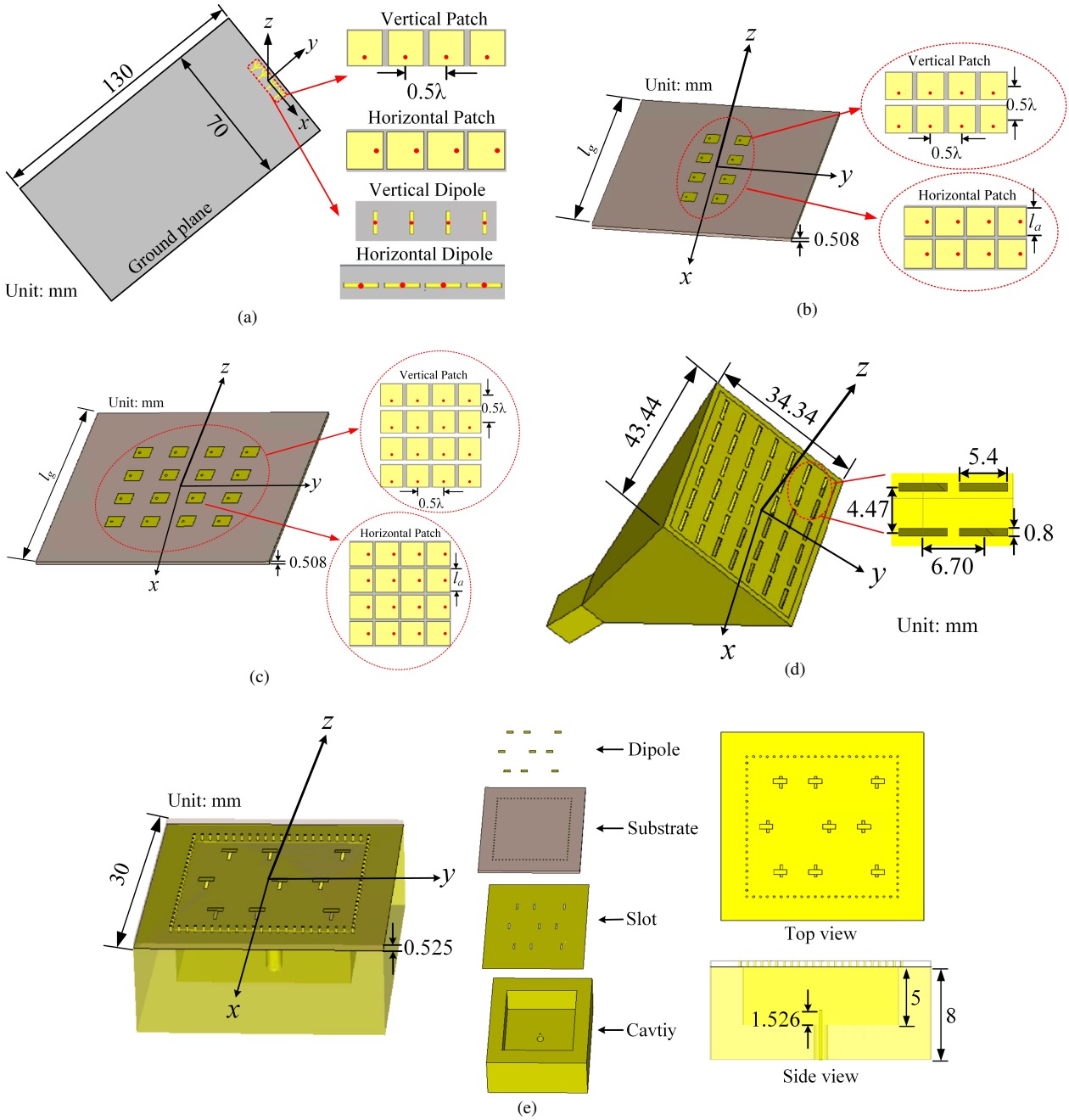

Fig. 4. Illustration of the simulated antenna arrays. (a) 1×4 dipole and patch antenna arrays for the operating frequencies of 28 GHz and 39 GHz in front of a 70 mm $\times$ 130 mm ground plane, in accordance with the current mobile terminal dimensions. The elements of the arrays include vertically and horizontally polarized half-wavelength dipole arrays and vertically and horizontally polarized half-wavelength patch arrays, where the red dots are feeding points. Antennas and ground plane are made of copper and presented in different colors for a better visualization. (b) 2×4 patch array for the operating frequencies of 28 GHz and 39 GHz. The element ($l_a \times l_a$, $l_a = 2.4$ mm for 28 GHz and $l_a = 2$ mm for 39 GHz) is printed on a substrate Rogers RO4350B (dimensions: $l_g \times l_g \times$ 0.508 mm, $l_g = 35$ mm for 28 GHz and $l_g = 25$ mm for 39 GHz, ε_r = 3.66, δ = 0.0037). (c) 4×4 patch array for operating frequencies of 28 GHz and 39 GHz. The element ($l_a \times l_a$) is printed on the same substrate as (b). (d) Horn-fed slot array for the operating frequency of 30 GHz. (e) Cavity-fed dipole array for the operating frequency of 30 GHz, the elements are printed on the substrate (ε_r = 3.63, δ = 0.0027). The inter-element spacing is 0.5λ, where λ is the free-space wavelength.

where $\hat{\boldsymbol{n}}$ is the unit vector normal to the area.

There has also been discussion, e.g., the technical report published by IEEE International Committee on Electromagnetic Safety (ICES) [27], on using the norm of the real part of the complex Poynting vector for EMF assessment,

$$S_{\text{inc},2} = \frac{1}{2}\|\text{Re}(\boldsymbol{E} \times \boldsymbol{H}^*)\|, \tag{5}$$

where $\|\cdot\|$ is the norm. This is because (5) also gives a good correlation with temperature rise on the body surface.

However, it should be noted that (5) does not have a real physical meaning as (4). Eq. (5) includes the tangential components and adds the absolute values of the energy flux in both directions rather than the net energy flux when integrating over an area.

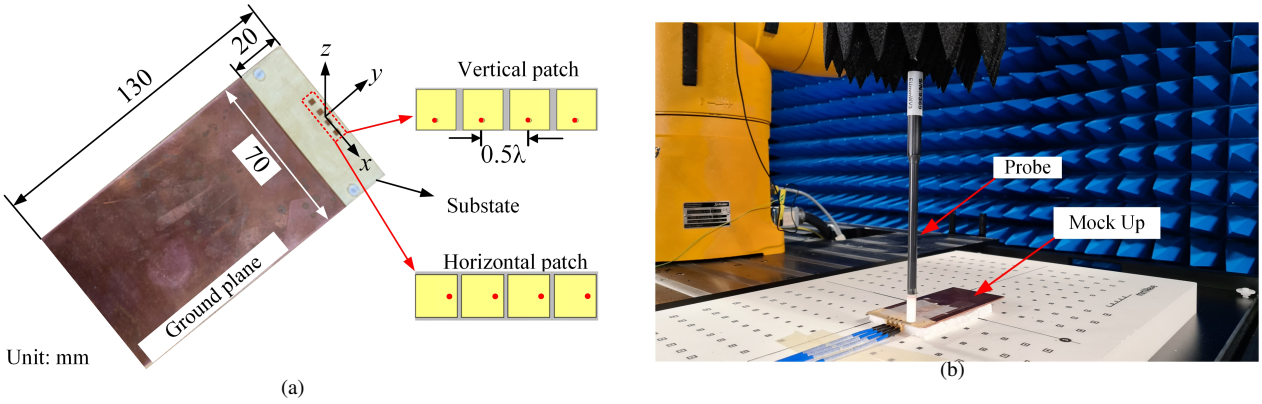

Fig. 5. (a) Mock-up of the 1×4 vertically and horizontally polarized patch arrays at the operating frequency of 28 GHz, and (b) measurement setup.

TABLE I
STUDIED EXPOSURE DISTANCES

Antenna	28 GHz	39 GHz
	Distance [mm]	
1×4 vertically polarized dipole array	1–25	
1×4 horizontally polarized dipole array		
1×4 vertically polarized patch array		
1×4 horizontally polarized patch array		
2×4 vertically polarized patch array	2–25	2–20
4×4 vertically polarized patch array	2–25, 28, 30, 35	2–25
2×4 horizontally polarized patch array	2–25	
4×4 horizontally polarized patch array	2–25, 28, 30, 35	
	30 GHz	
Horn-fed slot array	2–25, 35, 45, 55, 65, 70, 75	
Cavity-fed dipole array	2–25	

In [22], it is proposed to use the norm of the complex Poynting vector for IPD assessment

$$S_{\mathrm{inc},3} = \frac{1}{2}\|\boldsymbol{E} \times \boldsymbol{H}^*\|. \tag{6}$$

In addition to the problem of (5), (6) also includes the imaginary part. If the antenna is highly resonant with a large imaginary part and IPD is evaluated very close to the antenna, (6) will give very large non-physical results due to the imaginary part. Therefore, the imaginary part should not be used to define IPD.

B. Proposed Method to Determine Reactive Near-Field Boundary

Although the imaginary part is not equivalent to the reactive power at a single point, as indicated by Eq. (3), the decay of the imaginary part still indicates the decay of the reactive power. If the imaginary part is much smaller than the real part above certain distances, the reactive power may also be considered greatly reduced. Eqs. (4)–(6) converge when the evaluation distance approaches the far field, the differences between them are still small in the radiating near field, and finally the differences become largest in the reactive near field. Inspired by this, a new computational method of the boundary between the reactive and radiating near fields, $d_{\mathrm{ReNF_3}}$, is proposed by using the difference between $S_{\mathrm{inc},2}$ and $S_{\mathrm{inc},3}$

$$\Delta(x, y, z = d) = \frac{S_{\mathrm{inc},3}(x, y, d) - S_{\mathrm{inc},2}(x, y, d)}{\max\limits_{x,y} S_{\mathrm{inc},2}(x, y, d)}, \tag{7}$$

where d is the distance from the antenna to the evaluation plane. In (7), a parameter Δ is proposed to describe the additional contribution after considering the imaginary part of the Poynting vector (reactive power) compared to only counting on the real part of the Poynting vector for each single point. $d_{\mathrm{ReNF_3}}$ is the distance at which the peak value of Δ becomes

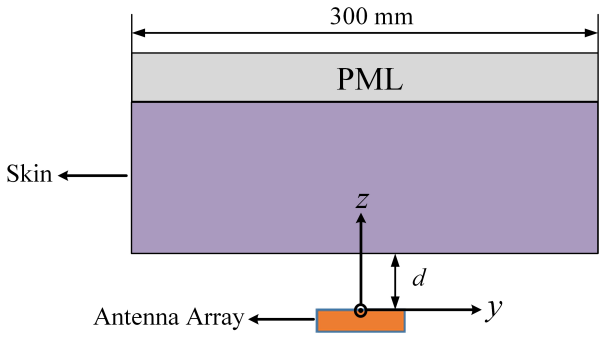

Fig. 6. The exposure scenario for APD evaluating with a phantom model.

TABLE II
PARAMETERS AND SIZE OF THE PHANTOM

Phantom Model	Parameters	Frequency		
		28 GHz	30 GHz	39 GHz
1-layer Skin	ϵ_r	17.1	16.63	12.4
	σ (S/m)	26.16	27.31	32.19
	Thickness (mm)	14	14	10
	Length (mm)	100–300		
	Width (mm)			

sufficiently small, or the variation of the peak Δ remains stable with increasing distances. As it is stated in IEC/IEEE 63195-1 ED1 [28], the point where the power density contributes to the spatial peak power density by $\leq 5\%$ can be ignored when combining power density for devices under test. According to this, in this study, the critical value of peak Δ for the reactive near-field boundary is set to 5%, as illustrated in Fig. 1. In the sections IIE, IIF, and IIG, the main lobes are towards $+z$-direction, and IPD is larger than in other directions. For other antennas and coordinate orientations, the coordinates in (7) must be changed accordingly. It should be highlighted again that this paper is to investigate the computational method of the reactive near-field boundary while the imaginary part of the Poynting vector should not used for any IPD definition.

C. Analytical Demonstration for The Proposed Reactive Near-Field Boundary

To analytically demonstrate the effectiveness of the proposed reactive near field boundary, an infinitesimal dipole operating at 28 GHz is used. The infinitesimal dipole, with a length of l = 0.01λ, is placed along the y-axis, as shown in Fig. 2. The evaluation plane at distance d from the infinitesimal dipole is $100\ \text{mm} \times 100\ \text{mm}$, the resolution is $0.01\ \text{mm}$. The electromagnetic fields on the evaluation plane with a distance d can be calculated by [23]

$$\boldsymbol{E}(x,y,z=d) = -j\omega \boldsymbol{A_{mag}}(x,y,z=d) - j\frac{1}{\omega\mu\epsilon}\nabla(\nabla\cdot\boldsymbol{A_{mag}}(x,y,z=d)), \quad (8)$$

$$\boldsymbol{H}(x,y,z=d) = \frac{1}{\mu}\nabla\times\boldsymbol{A_{mag}}(x,y,z=d), \quad (9)$$

where μ and ϵ are the permeability and permittivity in free space. $\boldsymbol{A_{mag}}$ is magnetic vector potential, which is defined as

$$\boldsymbol{A_{mag}}(x,y,z=d) = \hat{\boldsymbol{y}}\frac{\mu I_0 l}{4\pi \boldsymbol{r}} e^{-j\boldsymbol{kr}}, \quad (10)$$

where I_0 is the current along the infinitesimal dipole, and $\boldsymbol{k} = k_x\hat{\boldsymbol{x}} + k_y\hat{\boldsymbol{y}} + k_z\hat{\boldsymbol{z}}$, is the wave vector in free space. $\boldsymbol{r} = x\hat{\boldsymbol{x}} + y\hat{\boldsymbol{y}} + z\hat{\boldsymbol{z}}$, is the position coordinates. The Δ can be calculated for the infinitesimal dipole by (5)–(10).

On the other hand, electromagnetic waves can be represented as a superposition of plane waves with the same frequency propagating in different directions. For example, the electric field can be represented by [29]

$$\boldsymbol{E}(\boldsymbol{r}) = \frac{1}{4\pi^2}\int_{-\infty}^{\infty}\int_{-\infty}^{\infty}\tilde{\mathbf{E}}_{pw}(k_x,k_y)\, e^{-j\boldsymbol{k}\cdot\boldsymbol{r}} dk_x dk_y. \quad (11)$$

In (11), $\tilde{\mathbf{E}}_{pw}$ represents the plane wave spectrum of the electric field, which can be derived using the inverse Fourier transform

$$\tilde{\mathbf{E}}_{pw}(k_x,k_y) = \int_{-\infty}^{\infty}\int_{-\infty}^{\infty}\boldsymbol{E}(\boldsymbol{r})e^{j(k_x\cdot\boldsymbol{x}+k_y\cdot\boldsymbol{y}+k_z d)}dxdy. \quad (12)$$

The evanescent modes of $\tilde{\mathbf{E}}_{pw}$ are dominated in the reactive near field, and they will attenuate with an increasing distance. To calculate the evanescent modes, the wave number along the z direction requires $k_z^2 < 0$, i.e.,

$$k_z = \sqrt{k_x^2 + k_y^2 - k^2}. \quad (13)$$

Fig. 3 shows the evanescent modes of $\tilde{\mathbf{E}}_{pw}$ normalized to the maximum value (represented as 100% in the figure, corresponding to $d = 1$ mm), and the peak Δ as functions of an increasing distance. The units for both normalized evanescent modes of $\tilde{\mathbf{E}}_{pw}$ and peak Δ are percentage. It can be observed that the evanescent modes of $\tilde{\mathbf{E}}_{pw}$ remarkably attenuate when $d < 4$ mm, reaching a very small value and stabilized when $d \geq 4$ mm. This reflects the transition of the electromagnetic field from the reactive near field to the radiating near field. The curve for peak Δ closely overlaps with the curve for evanescent modes of $\tilde{\mathbf{E}}_{pw}$. The corresponding distance is close to 4 mm when the peak Δ is 5%. The same results of peak Δ and evanescent modes of $\tilde{\mathbf{H}}_{pw}$ can also be found for small loop antenna. They are not shown here for simplicity. From this perspective, the proposed boundary could represent the transition from the reactive near field to the radiation near field. In the following sections, the practical antennas and antenna arrays will be used to further demonstrate the proposed boundary as the criterion for applying IPD for EMF assessment, with APD as a benchmark.

D. Definition of APD

According to [2], APD, S_{ab}, is defined as

$$S_{\text{ab}} = \frac{1}{A}\iint_A dxdy\int_0^{z_{\max}} SAR(\boldsymbol{r})\rho(\boldsymbol{r})dz, \quad (14)$$

where the phantom surface is at z = 0, $z_{\max}$ is the depth of the human body phantom model, ρ is the mass density of the human body tissue. A is the averaging area ($4\ \text{cm}^2$ for 6 – 300 GHz and $1\ \text{cm}^2$ for 30 – 300 GHz [2]). SAR in (14) is defined as [2]

$$SAR(\boldsymbol{r}) = \frac{\sigma(\boldsymbol{r})}{2\rho(\boldsymbol{r})}\left|\boldsymbol{E}(\boldsymbol{r})\right|^2. \quad (15)$$

where σ is the electrical conductivity of the human body tissue. APD will be used as a benchmark for the study of the relationship between APD and IPD in Section IV.

E. Case Study for Practical Antennas/Antenna Arrays

In this case study, eight antenna arrays operating at 28 GHz, two antennas operating at 30 GHz, and six antenna arrays operating at 39 GHz are used, as shown in Fig. 4. The models of each antenna array are the following.

- 1×4 antenna array for the operating frequencies of 28 GHz and 39 GHz
  Four types of antenna arrays are used, including vertically and horizontally polarized half-wavelength dipole arrays and vertically and horizontally polarized half-wavelength patch arrays, as shown in Fig. 4(a). The inter-element spacing is 0.5λ, where λ is the free-space wavelength. The size of the ground plane behind each antenna array

(including patch and dipole arrays is $70\ \mathrm{mm}\times130\ \mathrm{mm}$, in accordance with the current mobile terminal dimensions. Between the antenna panel and the ground plane, low-lossy foam material is used to study the worst-case scenarios, meaning that the input power for the antenna will not attenuate caused by dielectric loss. Similar antenna settings can also be found in other studies, e.g., [30], [31]. For beam-scanning, the progressive phase shift of the antenna array, φ, is set to $0°$, $\pm30°$, $\pm60°$, $\pm90°$, and $\pm120°$.

- 2×4 and 4×4 patch array for the operating frequencies of 28 GHz and 39 GHz
  Two types of antenna arrays are used, including 2×4 and 4×4 vertically and horizontally polarized half-wavelength patch arrays, as shown in Fig. 4(b) and 4(c). For the frequency of 39 GHz, only the vertically polarized patch arrays will be considered for simplicity. The element ($l_a\times l_a$, $l_a = 2.4\mathrm{mm}$ for 28 GHz and $l_a = 2\mathrm{mm}$ for 39 GHz) is printed on a substrate Rogers RO4350B (dimensions: $l_g\times l_g\times0.508$ mm, $l_g = 35$ mm for 28 GHz and $l_g = 25$ mm for 39 GHz, ε_r = 3.66, δ = 0.0037). For beam-scanning, the progressive phase shifts settings are the same as 1×4 antenna arrays.
- Horn-fed slot array and cavity-fed dipole array for the operating frequency of 30 GHz
  The horn-fed slot array consists of a pyramidal horn loaded with a 6×7 slot array, as shown in Fig. 4(d). The dimension of each slot element is $5.4\ \mathrm{mm}\ \times 0.8\ \mathrm{mm}$, which is on the horn aperture. The aperture of the horn is $43.44\ \mathrm{mm}\times34.34\ \mathrm{mm}$. As shown in Fig. 4(e), the cavity-backed dipole array consists of 3×3 elements printed on a substrate (dimension: $30\ \mathrm{mm}\times30\ \mathrm{mm}$ ε_r = 3.63, δ = 0.0027). The detailed structure parameters of the horn-fed slot array and the cavity-fed dipole array can also be found in [28], [32], [33].

The total input power of each entire array is fixed to 23 dBm, i.e., 0.2 W, in accordance with the maximum allowed transmitted power for user equipment in the millimeter-wave (mmWave) spectrum [34]. The studied distances for each antenna or antenna array are shown in Table. I. To study the IPD, Δ, and APD in the following sections, the resolution is set to 0.1 mm for all antenna arrays operating at frequencies of 28 GHz, 30 GHz, and 39 GHz.

F. Measurement Setup

The IPD measurements on the manufactured 1×4 vertically and horizontally polarized patch antenna arrays operating at 28 GHz are performed in the semi-anechoic chamber. The arrays are printed on the substrate Rogers RO4350B (dimensions: 70 mm $\times$ 20 mm $\times$ 0.508 mm, ε_r = 3.66, δ = 0.0037) and the mock-ups are shown in Fig. 5(a). In the measurement setup in Fig. 5(b), the antenna-under-test (AUT) is placed above the SPEAG mmWave free-space phantom consisting of a 40 mm thick Rohacell plate with relative permittivity $\varepsilon_r \leq 1.2$ and loss tangent $\delta \leq 0.05$, which approximates free-space conditions without distorting the field. The electric field measurements are performed at 28 GHz in free space with the DASY6 mmWave module and the EUmmWV3 probe along three planes parallel to the AUT and for distances d of 4, 5, and 9 mm. The size of the measured planes is 70 mm $\times$ 50 mm centered at the center of the antenna array and the sampling step is $\lambda/4$. The electric and magnetic fields for the IPD evaluation were reconstructed through the equivalent source reconstruction (ESR) algorithm presented in [35].

G. Exposure scenario for APD Evaluating with A Phantom Model

As shown in Fig. 6, the one-layer tissue phantom, which only considers the skin is used in the APD computation. The reason is the penetration depth of the electromagnetic waves at 28 GHz, 30 GHz, and 39 GHz is mainly inside the skin layer. The permittivity and conductivity parameters of the phantom are interpolated using the data from [27]. They are shown in Table II, along with the size of the phantom. The same antennas in Section IIB will be reused in the APD computation at different antenna-to-phantom distances.

III. Simulation And Measurement Results

A. Comparisons of simulated Peak Δ and the normalized evanescent modes of $\tilde{\mathbf{E}}_{pw}$

Fig. 7 shows the distributions of $S_{\mathrm{inc},2}$, $S_{\mathrm{inc},3}$, and Δ at 1 mm for the studied horizontally polarized dipole arrays. It can be seen that the distributions of $S_{\mathrm{inc},2}$ and $S_{\mathrm{inc},3}$ are similar when $\varphi = 0°$, and the difference becomes larger when φ increases, i.e., the peak Δ increases from 44.8% to 79.3% when φ increases from $0°$ to $120°$. These findings can also be observed for the other studied patch and dipole antenna arrays in this paper, while they are not shown for simplicity.

Fig. 8 shows comparisons between evanescent modes of $\tilde{\mathbf{E}}_{pw}$ (percentage) normalized to the maximum value for each feeding phase shifts φ and peak Δ (percentage) as functions of distances. The scale for peak Δ is set to 0%–20% for better visualization. Different from Fig. 3, there are discrepancies between curves for normalized evanescent modes of $\tilde{\mathbf{E}}_{pw}$ and peak Δ for the practical antenna arrays. Nevertheless, the overall trend of the curve for peak Δ aligns with the curve for normalized evanescent modes of $\tilde{\mathbf{E}}_{pw}$. For example, for 1×4 vertically polarized patch array with $\varphi = 0°$shown in Fig. 8(a), peak Δ decreases by 85.7% (from 26.6% to 3.8%) as the separation distance increases from 2 mm to 7 mm ($d_{\mathrm{ReNF_3}}$), corresponding to 70.1% decrease in normalized evanescent modes of $\tilde{\mathbf{E}}_{pw}$ (from 100% to 29.9%). For larger array sizes, such as 2×4 and 4×4 vertically polarized patch arrays the attenuation of the normalized evanescent modes of $\tilde{\mathbf{E}}_{pw}$ become slower than the 1×4 patch array, which leads to a larger discrepancy between the curves for normalized evanescent modes of $\tilde{\mathbf{E}}_{pw}$ and peak Δ.

B. Determined Boundary $d_{\mathrm{ReNF_3}}$

Table III shows $d_{\mathrm{ReNF_3}}$ for different φ, frequencies, and polarization based on the results shown in Fig. 8. The following can be observed:

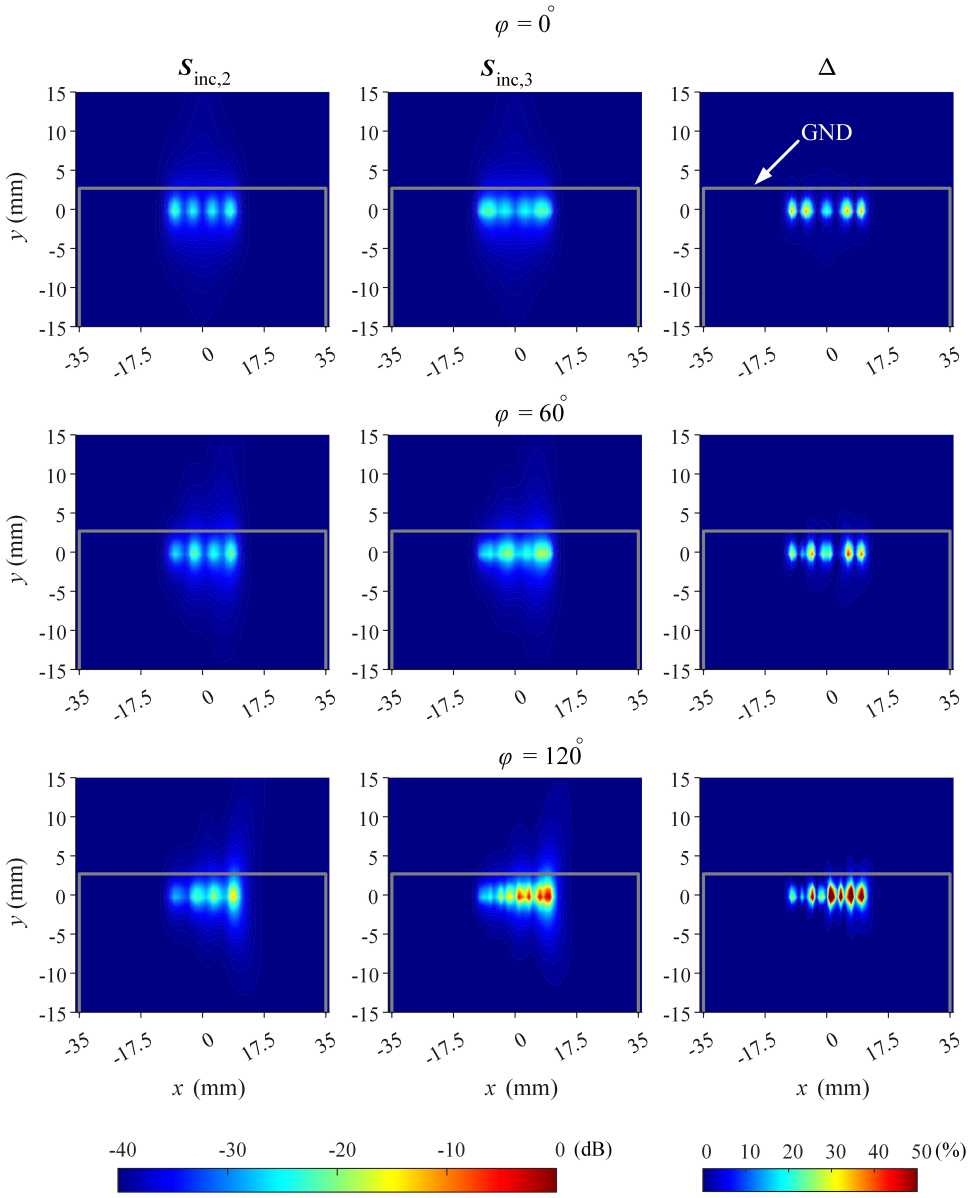

Fig. 7. Simulated distributions of $S_{\mathrm{inc},2}$, $S_{\mathrm{inc},3}$, and Δ at 1 mm away from the 1×4 horizontally polarized dipole array operating at 28 GHz with different phase shifts. $S_{\mathrm{inc},2}$ and $S_{\mathrm{inc},3}$ are normalized to the peak value. The unit of Δ is percentage. The gray lines represent the edges of the ground plane.

- For each array, $d_{\mathrm{ReNF_3}}$ is relatively stable for φ within $\pm 60°$, while it increases for the beams with larger scan angles.

- Comparing the vertically polarized arrays with the horizontally polarized arrays, the effects of polarization can result in different $d_{\mathrm{ReNF_3}}$ values. This may be attributed to the fact that the used horizontally polarized arrays have more mutual coupling between elements. The equivalent magnetic currents of the patch arrays are in parallel, and so do the electric current on dipoles for the horizontally polarized arrays. This leads to larger reactive energy, and thus larger reactive near-field boundaries.

- For the same type of antenna array at different frequencies, the ratio of $d_{\mathrm{ReNF_3}}$ to λ is approximately similar.

C. *Measured results for the normalized evanescent modes of $\tilde{\mathbf{E}}_{pw}$ and peak Δ*

Fig. 9 shows the evanescent modes of $\tilde{\mathbf{E}}_{pw}$ (percentage) normalized to the maximum value for each phase shifts φ, and peak Δ (percentage) using measured data for 1×4 patch arrays at the operating frequency of 28 GHz for different phase shifts of $\varphi = 0°$, $60°$, and $120°$ at d = 4, 5, and 9 mm. Similar to the discussion above, the overall trend of the curve for the peak Δ is roughly similar to the curve for the normalized evanescent modes of $\tilde{\mathbf{E}}_{pw}$, although there is a large discrepancy between the curves for the peak Δ and the normalized evanescent modes of $\tilde{\mathbf{E}}_{pw}$ when the feeding phase shifts $\varphi \neq 0°$. This discrepancy could be caused by the insufficient large measured planes.

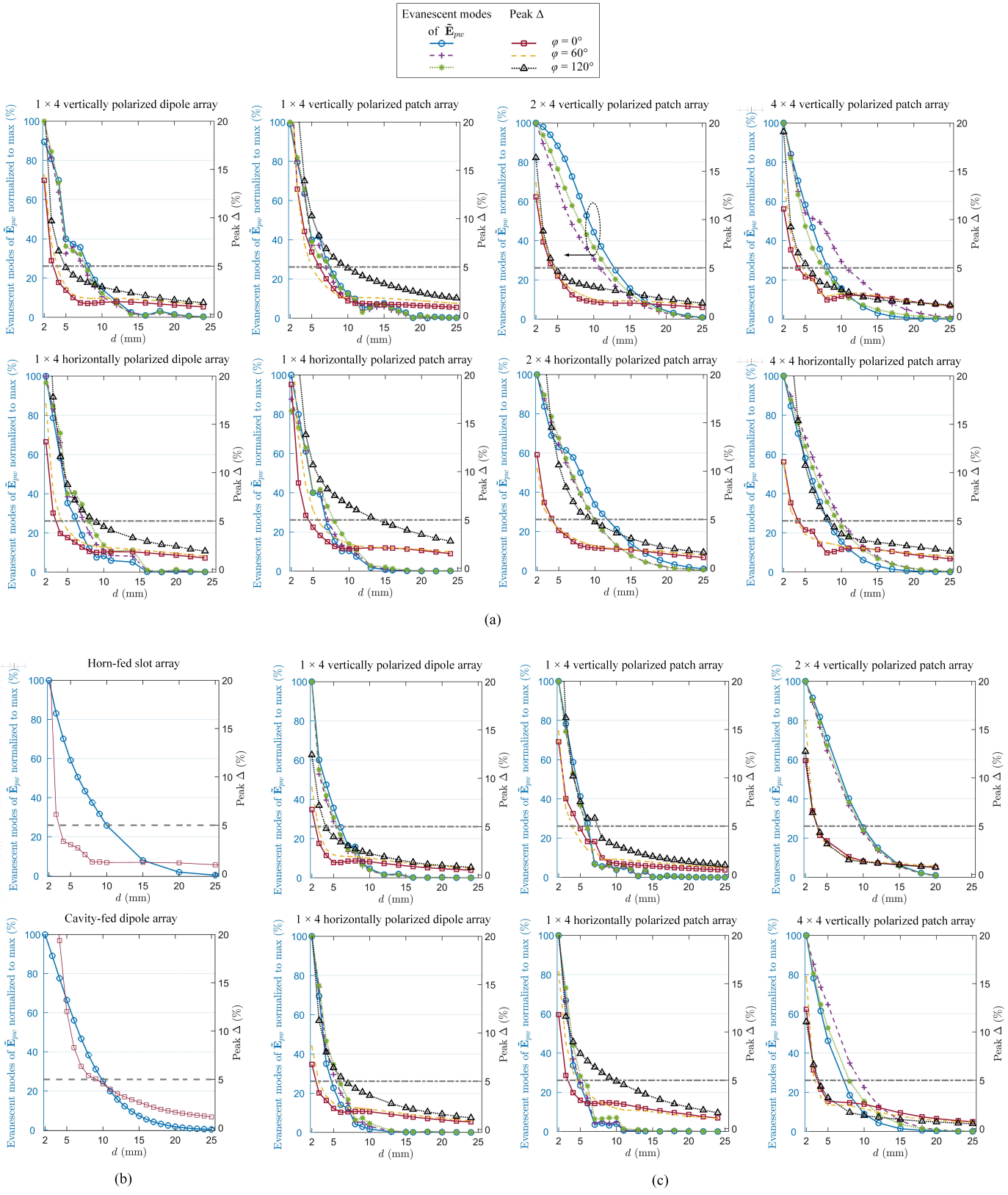

Fig. 8. The evanescent modes of $\tilde{\mathbf{E}}_{pw}$ (percentage) normalized to the maximum value for each feeding phase shifts φ and peak Δ (percentage) as functions of distances for the simulated antenna arrays, (a) vertically and horizontally polarized dipole and patch antenna arrays at the operating frequency of 28 GHz, (b) horn-fed slot and cavity-fed dipole arrays at the operating frequency of 30 GHz, (c) vertically and horizontally polarized dipole and patch arrays at the operating frequency of 39 GHz. The gray dashed line corresponds to 5%.

TABLE III
d_{ReNF_1},d_{ReNF_3}, AND d_{ReNF_2} FOR THE STUDIED PRACTICAL ANTENNA ARRAYS (UNIT: mm).

Antennas	28 GHz							39 GHz						
		Feeding phase shifts φ [°]							Feeding phase shifts φ [°]					
		0	30	60	90	120			0	30	60	90	120	
	d_{ReNF_1}	d_{ReNF_3}					d_{ReNF_2}	d_{ReNF_1}	d_{ReNF_3}					d_{ReNF_2}
1×4 vertically polarized dipole array	1.7	4	4	4	5	6	14	1.2	3	3	3	3	4	10
1×4 horizontally polarized dipole array		4	4	4	5	9	18		3	3	4	4	8	13
1×4 vertically polarized patch array		6	6	5	6	10	19		5	5	4	6	7	13
1×4 horizontally polarized patch array		5	5	5	7	13	20		4	4	4	6	9	14
2×4 vertically polarized patch array		5	5	5	5	5	18		4	4	4	4	4	13
4×4 vertically polarized patch array		4	5	5	5	6	26		4	4	4	3	4	19
2×4 horizontally polarized patch array		5	4	4	6	10	18							
4×4 horizontally polarized patch array		4	4	4	6	9	26							
	30 GHz													
Horn-fed slot array	1.6	4					65							
Cavity-fed dipole array		10					33							

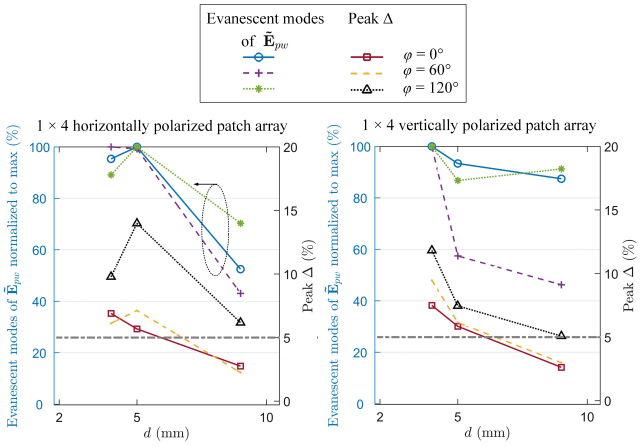

Fig. 9. The evanescent modes of $\tilde{\mathbf{E}}_{pw}$ (percentage) normalized to the maximum value for each feeding phase shifts φ and peak Δ (percentage) using measured data for 1×4 patch arrays at the operating frequency of 28 GHz for different phase shifts and distances.

IV. Effectiveness of The Proposed Boundary for Applying IPD as the Alternative to APD

As mentioned before, IPD cannot be used for the EMF assessment in the reactive near field where the reactive near-field boundary needs more studies for such applications [2]. The previous sections proposed a method to determine the reactive near-field boundary where the additional contribution after considering the imaginary part of the Poynting vector (reactive power) compared to only counting on the real part of the Poynting vector becomes significant ($> 5\%$). In this section, the relationship between IPD and APD inside and outside the proposed boundary is examined by setting APD as a benchmark. If IPD can be applied for EMF assessment, it should have a good correlation with APD, such as in the far field. If IPD starts to deviate from APD, it indicates that such close distances need to be considered as the reactive near field. For comparisons, $S_{\mathrm{inc},1}$, $S_{\mathrm{inc},2}$, and S_{ab} are averaged over the same size of A.

Fig. 10 presents the IPD and APD as functions of distances for the vertically polarized patch array operating at 28 GHz. It can be observed that S_{ab} decays with periodic oscillation when the distance is larger than around 5–7 mm. For closer distances, it is difficult to observe the oscillations, which indicates such a region is within the reactive near field. For S_{ab} with $\varphi = 120°$, oscillation can be clearly observed at $d >$ 10 mm. The distances where the oscillation behaviors can be clearly observed agree with the reactive near field boundary determined using the proposed method shown in Table III. Similar results can be found for other studied antennas in this paper, while they are not presented in the paper for simplicity.

Figs. 11–13 show the relationship between IPD and APD inside and outside the proposed boundary using a statistical approach. The aim is to further examine the relationship between IPD and APD. In Figs. 11 and 12, each scatterer represents the APD and IPD results at a specific d for a studied antenna operating at frequencies of 28 GHz, 30 GHz, and 39 GHz. The scatterers include data for all studied antenna arrays shown in Fig. 4, where the dipole and patch arrays are excited with feeding phase shifts of 0°, 30°, 60°, 90°, and 120°, at distances shown in Table. I. The scatterers are divided into three groups corresponding to $d > d_{\mathrm{ReNF}_2}$ (the squares, Group 1), $d_{\mathrm{ReNF}_3} < d < d_{\mathrm{ReNF}_2}$ (the triangles, Group 2), and $d_{\mathrm{ReNF}_1} < d < d_{\mathrm{ReNF}_3}$ (the dots, Group 3). The results in Group 1 are used for total least square (TLS) curve-fitting [36]–[38]. The TLS fitted line (the gray dashed line) shown in Figs. 11 and 12 is set as a benchmark to investigate the relationship between APD and IPD. From Figs. 11 and 12, it can be seen that the scatterers gradually deviate from the TLS fitted line from Group 1 to Group 3. In both Group 1 and Group 2, the scatterers are evenly distributed on both sides of the fitted line, and the other scatterers in Group 3 deviate significantly from the fitted line and mainly appear on one side

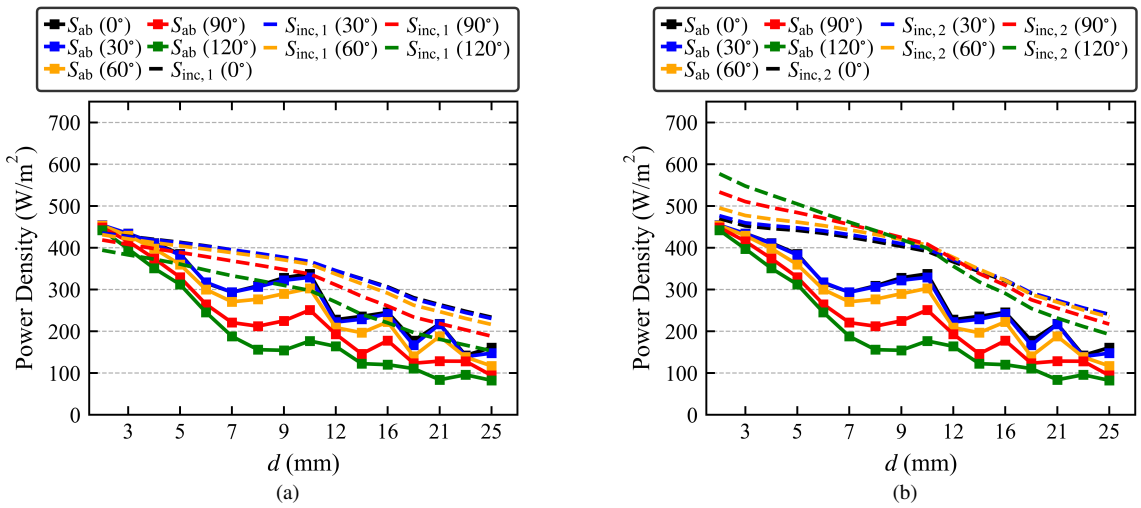

Fig. 10. APD and IPD averaged over $A = 4$ cm^2 for vertically polarized patch array operating at 28 GHz, excited with the feeding phase shifts of 0°, 30°, 60°, 90°, 120°. (a)$S_{\rm ab}$ and $S_{\rm inc,1}$, and (b)$S_{\rm ab}$ and $S_{\rm inc,2}$.

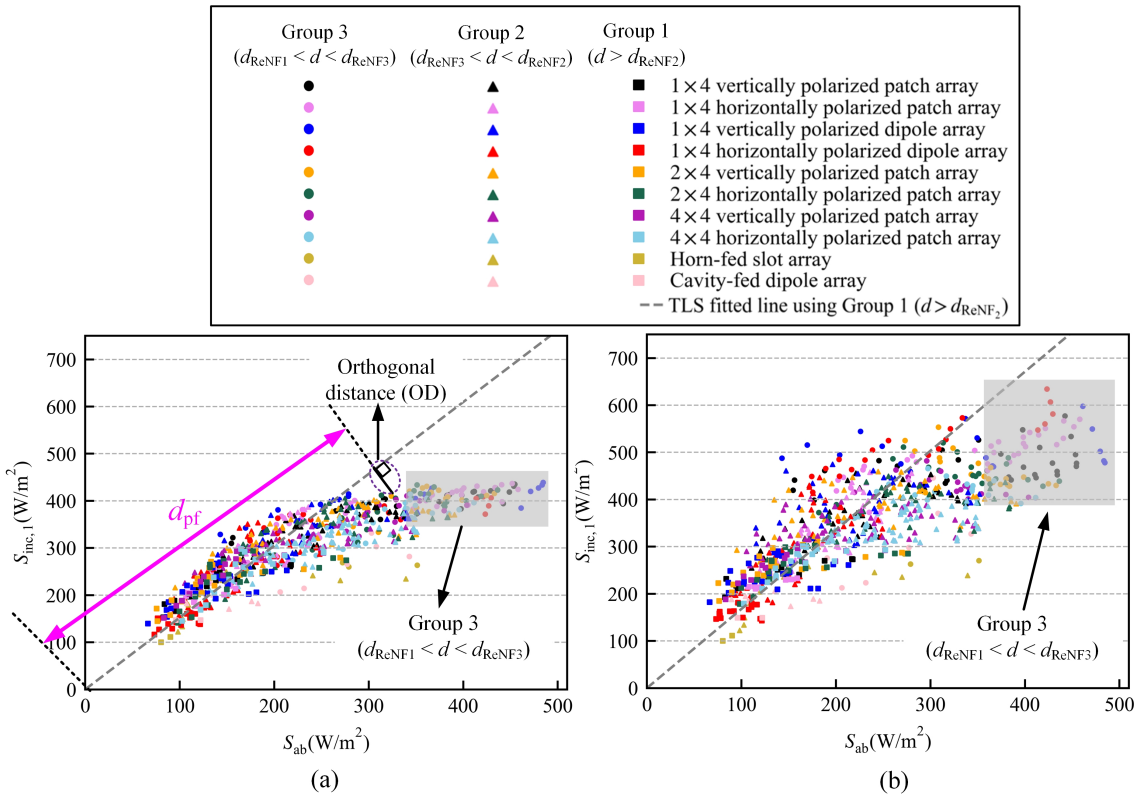

Fig. 11. APD versus IPD results for $A = 4$ cm^2 and operating frequencies of 28 GHz and 30 GHz. Each scatterer represents the APD and IPD results at a specific d for a studied antenna. The scatterers include data for all studied antenna arrays, which also includes the data for patch and dipole arrays excited with different feeding phase shifts of 0°, 30°, 60°, 90°, and 120°. The gray dashed line is the total least square (TLS) fitted curve using the data from Group 1. The shadow region includes the most scatterers in Group 3. These scatterers deviate from the TLS fitted curve. OD is the orthogonal distance from the corresponding scatterer to the TLS fitted line, and $d_{\rm pf}$ is the intercept of the projection point of the scatterer onto the TLS fitted line. OD and $d_{\rm pf}$ will be used in Fig. 13 to quantify the deviation of the scatterers from the TLS fitted line. (a) $S_{\rm ab}$ versus $S_{\rm inc,1}$, and (b) $S_{\rm ab}$ versus $S_{\rm inc,2}$.

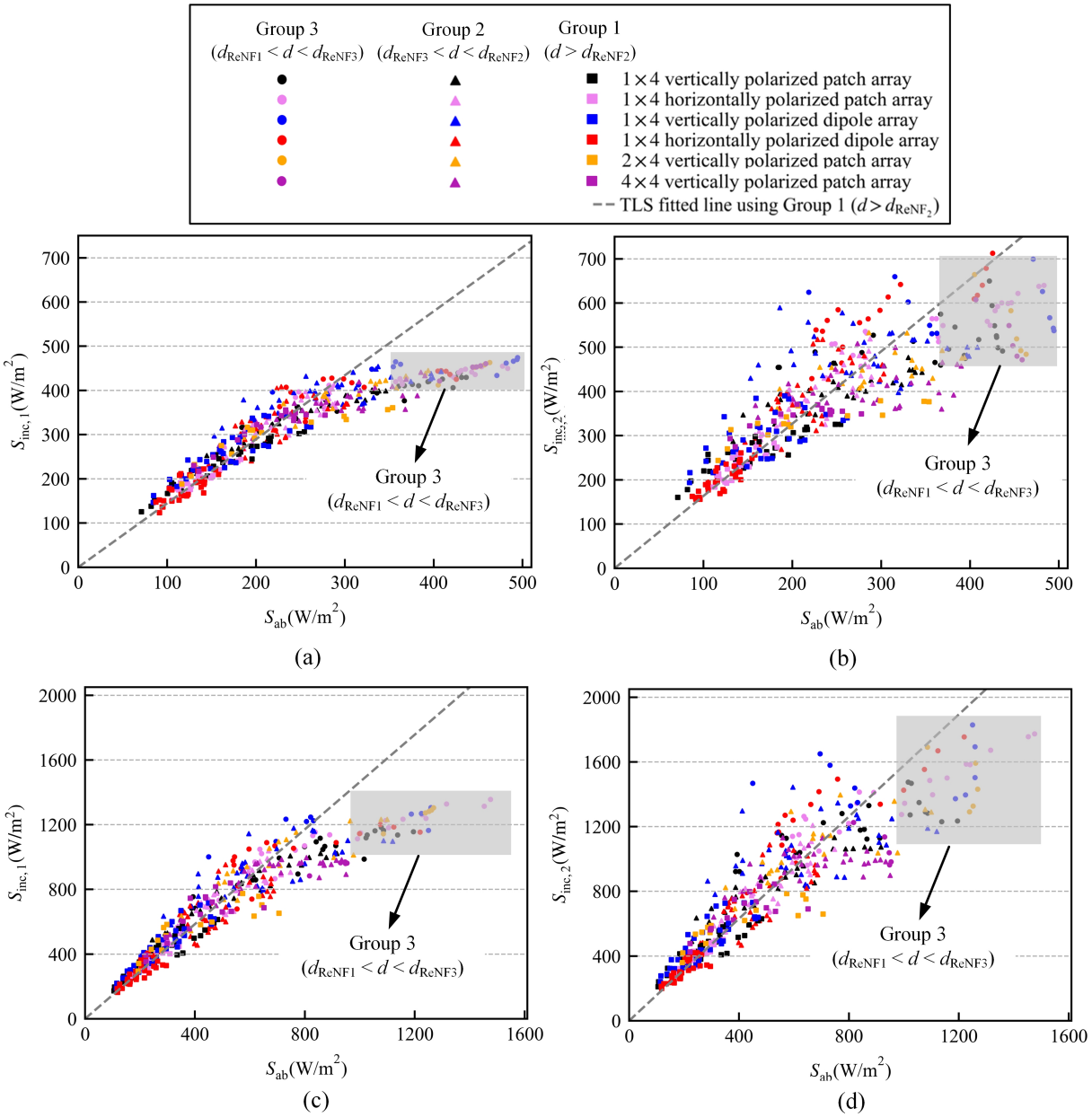

Fig. 12. APD versus IPD results for the operating frequency of 39 GHz. Each scatterer represents the APD and IPD results at a specific d for a studied antenna at 39 GHz. The scatterers include data for all studied antenna arrays excited with feeding phase shifts of 0°, 30°, 60°, 90°, and 120°. The gray dashed line is the TLS fitted curve using the data from Group 1. The shadow region includes the most scatterers in Group 3. These scatterers deviate from the TLS fitted curve.(a) $S_{\rm ab}$ versus $S_{\rm inc,1}$ for $A = 4$ cm^2, (b) $S_{\rm ab}$ versus $S_{\rm inc,2}$ for $A = 4$ cm^2, (c) $S_{\rm ab}$ versus $S_{\rm inc,1}$ for $A = 1$ cm^2, and (d) $S_{\rm ab}$ versus $S_{\rm inc,2}$ for $A = 1$ cm^2.

of the fitted line regardless of the frequency and averaging area.

To further quantify the deviation from the TLS fitted line, the normalized orthogonal distance β calculated for each group is presented in Fig. 13. β is defined by

$$\beta = \frac{OD}{d_{\rm pf}}, \tag{16}$$

where OD is the orthogonal distance from the corresponding scatterer to the TLS fitted line, and $d_{\rm pf}$ is the intercept of the projection point of the scatterer onto the TLS fitted line, as shown in Fig. 11(a). In Fig. 13, the mean of β is calculated using the results in Figs. 11 and 12 for each group. For $S_{\rm ab}$ versus $S_{\rm inc,1}$ at 28 and 30 GHz, there is around 10% difference in the mean of β between Group 1 and Group 2, which is marginal. However, the mean of β has a larger increase (74.4%, from 0.080 to 0.141) from Group 2 to Group 3. For $S_{\rm ab}$ versus $S_{\rm inc,2}$ at 28 and 30 GHz, the mean of β increases by 10% (from 0.081 to 0.091) from Group 1 to Group 2, which is similar to the case of $S_{\rm ab}$ versus $S_{\rm inc,1}$. From Group 2 to Group 3, the mean of β increases by 28.8% (from 0.091 to 0.118), which is smaller compared to the case of $S_{\rm ab}$ versus $S_{\rm inc,1}$. Similar results can be found for 39 GHz. For both $S_{\rm ab}$ versus $S_{\rm inc,1}$ and $S_{\rm ab}$ versus $S_{\rm inc,2}$ cases, a more substantial

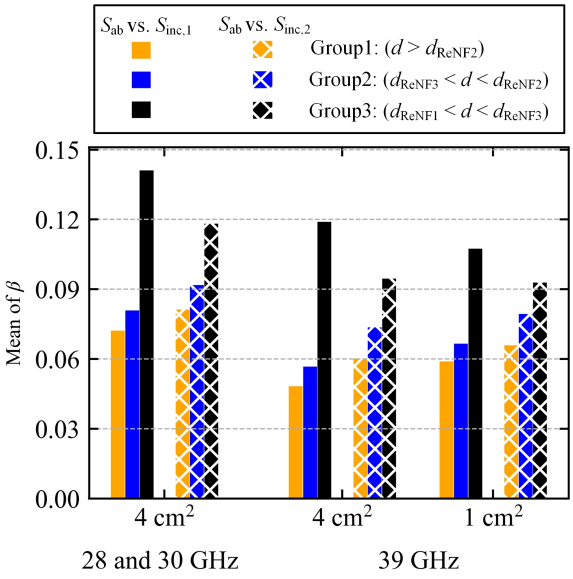

Fig. 13. Mean of β with respect to the TLS fitted line using the data shown in Figs. 11 and 12. β is defined by OD/d_{pf}, where OD and d_{pf} are as shown in Fig. 11(a).

increase in the mean of β from Group 2 to Group 3 compared to that from Group 1 to Group2 quantitatively indicates the significant deviation of the points from the TLS fitted line, which agrees with what can be observed in Figs. 11 and 12.

V. Discussion and Conclusions

In this study, we proposed a method to determine the reactive near-field boundary for applying IPD for EMF assessment of practical devices under test. This boundary is defined as the distance where the additional contribution after considering the imaginary part of the Poynting vector (reactive power) compared to only counting on the real part of the Poynting vector becomes significant. In this method, the parameter Δ is proposed to describe the additional contribution after considering the imaginary part of the Poynting vector (reactive power) compared to only counting on the real part of the Poynting vector.

The boundary is defined as the distance where the peak value of Δ becomes sufficiently small and the variation of peak Δ remains stable with increasing distances. The boundary determination requires electromagnetic fields at different distances, and in practice, the evaluation of the electromagnetic fields can be efficiently performed to decide the proposed boundary using fast assessment algorithms, e.g., [29], [32], [39]–[44]. The effectiveness of this boundary is demonstrated from two perspectives:

1). The comparisons in the trend of the curves between the peak Δ and evanescent modes of $\tilde{\mathbf{E}}_{pw}$ and $\tilde{\mathbf{H}}_{pw}$, where the infinitesimal dipole, small loop, and sixteen practical antenna arrays are used. The analytical, simulated, and measured results show that the proposed method can describe the transition from the reactive near fields to the radiation near field.

2). The correlation between IPD and APD. Sixteen practical antenna arrays at operating frequencies of 28 GHz, 30 GHz, and 39 GHz are used to examine whether IPD can be applied to EMF assessment inside and outside the proposed boundary by setting APD as a benchmark.

Figs. 3, 8, and 9 show that the overall trend of the curve for peak Δ with an increasing distance is roughly similar to the normalized evanescent modes of $\tilde{\mathbf{E}}_{pw}$, although there are some discrepancies for large antenna arrays sizes, such as 2×4 and 4×4 patch arrays and horn-fed slot array.

In Figs. 11-13, we divided data into three groups for three regions using the boundaries determined by (1), (7), and (2). The aim is to examine the correlation between APD and IPD across various regions determined by the classical and proposed methods. It can be seen that the scatterers in Group 1 and Group 2 appear evenly on both sides of the TLS fitted line as the APD decays similarly to IPD outside the reactive near field with extra oscillation. The scatterers in Group 3 ($d < d_{\mathrm{ReNF},3}$) mainly appear on one side of the TLS fitted line and the β to the fitted line becomes large. It indicates that the antenna-to-phantom interaction is dominated by reactive energy. From this perspective, the proposed boundary could better represent the transition region from the reactive near field to the radiating near field compared to the boundary determined using (1) and (2). IPD has a good correlation with APD outside the proposed boundary.

Although the findings are observed from the limited examples, the study and analysis method can be applied to any type of antennas, and provide a research perspective for determining whether IPD can be used for EMF compliance assessment in the near field.

Acknowledgment

The authors would like to thank Kenneth H. Joyner at Mobile & Wireless Forum, Kai Niskala at Samsung Electronics Co. Ltd., Stanislav Stefanov Zhekov, Carla Di Paola and Bo Xu at Ericsson Research, Ericsson AB, Kun Zhao and Zhinong Ying at Sony Corporation for the helpful ideas, suggestions, and discussions throughout the investigations.

References

[1] A. Hirata *et al.*, "Assessment of human exposure to electromagnetic fields: Review and future directions," *IEEE Trans. Electromagn. Compat.*, vol. 63, no. 5, pp. 1619–1630, 2021.

[2] International Commission on Non-Ionizing Radiation Protection(ICNIRP), "Guidelines for limiting exposure to electromagnetic fields (100 kHz to 300 GHz)," *Health Phys.*, vol. 118, no. 5, pp. 483–524, 2020.

[3] K. Taguchi, S. Kodera, A. Hirata, and T. Kashiwa, "Computation of absorbed power densities in high-resolution head models by considering skin thickness in quasi-millimeter and millimeter wave bands," *IEEE Journal of Electromagnetics, RF and Microwaves in Medicine and Biology*, vol. 6, no. 4, pp. 516–523, 2022.

[4] K. Li, S. Kodera, D. Poljak, Y. Diao, K. Sasaki, A. Šušnjara, A. Prokop, K. Taguchi, J. Xi, S. Zhang, M. Yao, G. Sacco, M. Zhadobov, W. E. Hajj, and A. Hirata, "Calculated Epithelial/Absorbed Power Density for Exposure From Antennas at 10–90 GHz: Intercomparison Study Using a Planar Skin Model," *IEEE Access*, vol. 11, pp. 7420–7435, 2023.

[5] K. Sasaki, M. Mizuno, K. Wake, and S. Watanabe, "Monte Carlo simulations of skin exposure to electromagnetic field from 10 GHz to 1 THz," *Phys. Med. Biol.*, vol. 62, no. 17, p. 6993, 2017.

[6] D. Funahashi, A. Hirata, S. Kodera, and K. R. Foster, "Area-averaged transmitted power density at skin surface as metric to estimate surface temperature elevation," *IEEE Access*, vol. 6, pp. 77 665–77 674, 2018.

[7] N. Miura, S. Kodera, Y. Diao, J. Higashiyama, Y. Suzuki, and A. Hirata, "Power Absorption and Skin Temperature Rise From Simultaneous Near-Field Exposure at 2 and 28 GHz," *IEEE Access*, vol. 9, pp. 152 140–152 149, 2021.

[8] Y. Diao, E. A. Rashed, and A. Hirata, "Assessment of absorbed power density and temperature rise for nonplanar body model under electromagnetic exposure above 6 GHz," *Phys. Med. Biol.*, vol. 65, no. 22, p. 224001, 2020.

[9] Y. Diao and A. Hirata, "Exposure Assessment of Array Antennas at 28 GHz Using Hybrid Spherical Near-Field Transformation and FDTD Method," *IEEE Trans. Electromagn. Compat.*, vol. 63, no. 5, pp. 1690–1698, 2021.

[10] M. Yao, S. S. Zhekov, B. Xu, K. Li, and S. Zhang, "A Study on Exposure to Electromagnetic Fields From User Equipment Antennas Above 100 GHz," *IEEE Trans. Electromagn. Compat.*, pp. 1–8, 2023.

[11] K. Li, "Multivariate regression analysis of skin temperature rises for millimeter-wave dosimetry," *IEEE Trans. Electromagn. Compat.*, vol. 64, no. 4, pp. 941–950, 2022.

[12] K. Li, K. Sasaki, S. Watanabe, and H. Shirai, "Relationship between power density and surface temperature elevation for human skin exposure to electromagnetic waves with oblique incidence angle from 6 GHz to 1 THz," *Phys. Med. Biol.*, vol. 64, no. 6, p. 065016, 2019.

[13] A. L. Kapetanović and D. Poljak, "Assessment of Incident Power Density on Spherical Head Model up to 100 GHz," *IEEE Trans. Electromagn. Compat.*, vol. 64, no. 5, pp. 1296–1303, 2022.

[14] T. Nakae, D. Funahashi, J. Higashiyama, T. Onishi, and A. Hirata, "Skin Temperature Elevation for Incident Power Densities From Dipole Arrays at 28 GHz," *IEEE Access*, vol. 8, pp. 26 863–26 871, 2020.

[15] B. Xu, K. Zhao, Z. Ying, D. Sjöberg, W. He, and S. He, "Analysis of Impacts of Expected RF EMF Exposure Restrictions on Peak EIRP of 5G User Equipment at 28 GHz and 39 GHz Bands," *IEEE Access*, vol. 7, pp. 20 996–21 005, 2019.

[16] W. He, B. Xu, Y. Yao, D. Colombi, Z. Ying, and S. He, "Implications of Incident Power Density Limits on Power and EIRP Levels of 5G Millimeter-Wave User Equipment," *IEEE Access*, vol. 8, pp. 148 214–148 225, 2020.

[17] K. Li, Y. Diao, K. Sasaki, A. Prokop, D. Poljak, V. Doric, J. Xi, S. Kodera, A. Hirata, and W. E. Hajj, "Intercomparison of Calculated Incident Power Density and Temperature Rise for Exposure From Different Antennas at 10–90 GHz," *IEEE Access*, vol. 9, pp. 151 654–151 666, 2021.

[18] W. He, B. Xu, M. Gustafsson, Z. Ying, and S. He, "RF Compliance Study of Temperature Elevation in Human Head Model Around 28 GHz for 5G User Equipment Application: Simulation Analysis," *IEEE Access*, vol. 6, pp. 830–838, 2018.

[19] V. De Santis, A. D. Francesco, G. Bit-Babik, J. Roman, and W. E. Hajj, "On the Correlation Between Incident Power Density and Temperature Increase for Exposures at Frequencies Above 6 GHz," *IEEE Access*, vol. 10, pp. 82 236–82 245, 2022.

[20] K. Li, K. Sasaki, K. Wake, T. Onishi, and S. Watanabe, "Quantitative Comparison of Power Densities Related to Electromagnetic Near-Field Exposures With Safety Guidelines From 6 to 100 GHz," *IEEE Access*, vol. 9, pp. 115 801–115 812, 2021.

[21] Y. Diao, K. Li, K. Sasaki, S. Kodera, I. Laakso, W. E. Hajj, and A. Hirata, "Effect of incidence angle on the spatial-average of incident power density definition to correlate skin temperature rise for millimeter wave exposures," *IEEE Trans. Electromagn. Compat.*, vol. 63, no. 5, pp. 1709–1716, 2021.

[22] A. Christ, T. Samaras, E. Neufeld, and N. Kuster, "Limitations of incident power density as a proxy for induced electromagnetic fields," *Bioelectromagnetics*, vol. 41, no. 5, pp. 348–359, 2020.

[23] C. A. Balanis, *Antenna theory: analysis and design*. John wiley & sons, 2015.

[24] W. L. Stutzman and G. A. Thiele, *Antenna Theory Design*. New York, NY, USA:Wiley, 2012.

[25] P. Baumgartner, T. Bauernfeind, W. Renhart, and O. Bíró, "Numerical investigations of the field regions for wire-based antenna systems," *IEEE Transactions on Magnetics*, vol. 56, no. 3, pp. 1–4, 2020.

[26] R. Collin and S. Rothschild, "Evaluation of antenna Q," *IEEE Trans. Antennas Propag.*, vol. 12, no. 1, pp. 23–27, 1964.

[27] "IEEE guide for the definition of incident power density to correlate surface temperature elevation," IEEE, Tech. Rep. IEEE 2889-2021, Dec. 2021.

[28] IEC/IEEE 63195-1 ED1, *Assessment of power density of human exposure to radio frequency fields from wireless devices in close proximity to the head and body (Frequency range of 6 GHz to 300 GHz) – Part 1: Measurement procedure*, 106/507/FDIS, 2021.

[29] K. Sasaki, K. Li, J. Chakarothai, T. Iyama, T. Onishi, and S. Watanabe, "Error analysis of a near-field reconstruction technique based on plane wave spectrum expansion for power density assessment above 6 GHz," *IEEE Access*, vol. 7, pp. 11 591–11 598, 2019.

[30] S. S. Zhekov, K. Zhao, O. Franek, and S. Zhang, "Test reduction for power density emitted by handset mmwave antenna arrays," *IEEE Access*, vol. 9, pp. 23 127–23 138, 2021.

[31] S. S. Zhekov, M. Yao, O. Franek, K. Zhao, and S. Zhang, "EMF Exposure of Human Head by Handset mmWave Phased Antenna Array," in *Proc. 16th Eur. Conf. Antennas Propag. (EuCAP)*, 2022, pp. 1–5.

[32] S. Pfeifer, E. Carrasco, P. Crespo-Valero, E. Neufeld, S. Kuhn, T. Samaras, A. Christ, M. H. Capstick, and N. Kuster, "Total field reconstruction in the near field using pseudo-vector E-field measurements," *IEEE Trans. Electromagn. Compat.*, vol. 61, no. 2, pp. 476–486, 2019.

[33] *Measurement Procedure for the Evaluation of Power Density Related to Human Exposure to Radio Frequency Fields From Wireless Communication Devices Operating Between 6 GHz and 100 GHz*, vol. document IEC TR 63170 ED1, 2018.

[34] *User Equipment (UE) radio transmission and reception; Part 2: Range 2,* Standalone, Standard TS 38.101-2, 3GPP, Rev. 16.0.0, Jun., 2019.

[35] K. S. Cujia, A. Fallahi, S. Reboux, and N. Kuster, "Experimental exposure evaluation from the very close near-to the far-field using a multiple-multipole source reconstruction algorithm," *IEEE Trans. Antennas Propag.*, 2022.

[36] G. H. Golub and C. F. V. Loan, "An analysis of the total least squares problem," *Numer. Anal.*, vol. 17, pp. 883–893, 1980.

[37] P. de Groen, "An introduction to total least squares," *Nieuw Archief voor Wiskunde*, vol. 14, no. 2, pp. 237–254, July 1996.

[38] I. Markovsky and S. V. Huffel, "Overview of total least-squares methods," *Signal Process.*, vol. 87, no. 10, pp. 2283–2302, 2007.

[39] S. Pfeifer, A. Fallahi, J. Xi, E. Neufeld, and N. Kuster, "Forward transformation from reactive near-field to near and far-field at millimeter-wave frequencies," *Appl. Sci.*, vol. 10, no. 14, p. 4780, 2020.

[40] K. Sasaki, K. Li, K. Wake, S. Watanabe, J. Higashiyama, and T. Onishi, "Accuracy of incident power density measured using reconstructing algorithm for compliance assessment of devices in near-field at millimeter-wave frequencies," in *Proc. Joint Int. Symp. Electromagn. Compat.*, 2019, pp. 43–46.

[41] Y. Diao and A. Hirata, "Assessment of mmwave exposure from antenna based on transformation of spherical wave expansion to plane wave expansion," *IEEE Access*, vol. 9, pp. 111 608–111 615, 2021.

[42] J. Lundgren, J. Helander, M. Gustafsson, D. Sjoberg, B. Xu, and D. Colombi, "A near-field measurement and calibration technique: Radio-frequency electromagnetic field exposure assessment of millimeter-wave 5G devices," *IEEE Antennas Propag. Mag.*, vol. 63, no. 3, pp. 77–88, 2021.

[43] K. S. Cujia, A. Fallahi, S. Reboux, and N. Kuster, "Experimental exposure evaluation from the very close near-to the far-field using a multiple-multipole source reconstruction algorithm," *IEEE Trans. Antennas Propag.*, vol. 70, no. 9, pp. 8461–8472, 2022.

[44] W. He, B. Xu, L. Scialacqua, Z. Ying, A. Scannavini, L. J. Foged, K. Zhao, C. Di Paola, S. Zhang, and S. He, "Fast Power Density Assessment of 5G Mobile Handset Using Equivalent Currents Method," *IEEE Trans. Antennas Propag.*, vol. 69, no. 10, pp. 6857–6869, 2021.